Modulated-photocurrent spectroscopy of single-crystal organic semiconductor rubrene with pristine and trap-dominated surfaces

N. Vagenas,[1] V. Podzorov,[2] and P. Kounavis[1,*]

[1]*Department of Electrical and Computer Engineering, University of Patras, 26504, Patra, Greece*

[2]*Department of Physics and Astronomy, Rutgers University, Piscataway, New Jersey 08854, USA*

(Received 24 September 2020; revised 23 April 2021; accepted 18 May 2021; published 1 June 2021)

High-performance, benchmark organic semiconductor rubrene is investigated by modulated-photocurrent (MPC) spectroscopy. In this technique, periodically modulated and steady-state photocarrier populations are simultaneously generated in the sample by two independent light beams, with the resultant photocurrent measured by a lock-in amplifier. The technique allows identifying a bandlike carrier motion (as opposed to incoherent hopping) as the dominant charge transport mechanism in this highly crystalline molecular semiconductor, in agreement with prior studies, yet without the need for fabrication of complex transistor devices. Moreover, MPC spectroscopy is used to determine the important parameters, such as the density of states for traps, their carrier capture coefficient, and attempt to escape frequency, as well as the quantum efficiency of photocarrier generation and the photocarrier mobility. The MPC spectroscopy is also shown to be able to discriminate charge transport at the surface of the crystal from that occurring in the bulk. The wealth of the thus obtained information is essential for our better understanding of the microscopic mechanisms governing photoconductivity in this class of materials.

DOI: 10.1103/PhysRevMaterials.5.063801

I. INTRODUCTION

High-purity single crystals of a small-molecule organic semiconductor rubrene ($C_{42}H_{28}$) exhibit comparatively high photoconductivity (PC) in the visible spectral range, for wavelengths $400 < \lambda < 560$ nm, where rubrene is an efficient light absorber. A variety of optoelectronic devices based on crystalline organic semiconductors, including photodetectors and solar cells, are envisioned [1–9]. It would thus be very important to understand the fundamental processes of photocarrier generation, transport, and charge interactions with traps in benchmark organic semiconductors, such as rubrene. Modulated-photocurrent (MPC) spectroscopy is a technique that has been proven powerful for investigating the interactions of majority carriers with traps in inorganic semiconductors [10]. More recently, MPC spectroscopy has been also applied to polycrystalline thin films of pentacene ($C_{22}H_{14}$), in which it allowed determining the dominant transport mechanism, extracting the distribution of trap states, and evaluating the impact of steady-state illumination on charge carrier mobility [11].

Here MPC measurements are carried out in a crystalline, high-performance organic semiconductor (rubrene). In this technique, a sample is illuminated with a monochromatic beam of light periodically modulated at a frequency ω (the so-called "probe" beam), and an ac photocurrent generated by this beam is detected by a lock-in amplifier tuned to the same frequency. This phase-sensitive detection technique allows one to significantly improve the signal to noise ratio in measurements of photoconductivity. Simultaneously, the sample is subjected to an additional continuous-wave (cw) photoexcitation with a secondary light beam (called a "bias" beam). The additional excitation can affect the properties of photocarriers generated by the probe. The relative phase and amplitude of the thus obtained ac photoconductivity, recorded under a cw bias beam of varied intensity, carry the information about the mobility of photocarriers, their transport mechanism, the density of states (DOS), and the carrier capture coefficient and attempt to escape frequency of localized states (traps) in the semiconductor's band gap. For instance, we demonstrate that a very interesting effect of degradation of organic semiconductors in high-vacuum chambers, called a "gauge effect," can be efficiently studied by the MPC technique. The gauge effect refers to a drastic deterioration of the charge transport characteristics of organic semiconductors' surfaces induced by exposure of a sample to an operating high-vacuum pressure gauge [12]. We reveal in detail the changes induced by the gauge effect in rubrene's DOS of traps, their capture coefficient, and the charge carrier mobility, as well as the quantum efficiency of photocarrier generation.

II. EXPERIMENTAL SECTION

A. Sample preparation

Rubrene single crystals with typical dimensions of (***a***,***b***) facets in the range 1–3 mm and thickness 0.1–1 mm were grown by a physical vapor transport following the previously published procedure [13]. Selected single crystals with well-defined facets were attached to substrates using tiny droplets of rubber cement glue, and two contacts were painted with

*Corresponding author: pkounavis@upatras.gr

an aqueous suspension of colloidal graphite (carbon paint) that upon drying provides a good electrical contact to rubrene. Device wiring was done using a 25 μm thick gold wire.

B. Photocurrent excitation spectroscopy

Photocurrent excitation (PCE) spectroscopy was carried out under cw illumination. The source of illumination was a monochromatic output from a Cornerstone-Oriel monochromator passed through a filter and focused on the crystal. During the PCE measurements, the crystal was kept in an optical cryostat at $\sim 10^{-1}$ Torr. The intensity (or power density) F of the incident light was tuned by using neutral density filters and measured with a calibrated photodetector. A small dc source-drain voltage, $V_{SD} \approx 1$–5 V, was applied between the graphite contacts with a Keithley 2400 source meter, and the resulting photocurrent, I_{SD}, flowing through the crystal was measured with a Keithley 617 or 6517B electrometer.

C. Modulated-photocurrent (MPC) spectroscopy

In the MPC measurements, the input voltage of a blue light emitting diode (LED) ($\lambda = 460$ nm) is sinusoidally modulated and the resulting modulated light emitted from the LED at a frequency in the range $\omega = 0.8$–10^5 Hz is used as the probe beam. The beam is incident at a free (***a***,***b***) facet of a rubrene single crystal, as schematically shown in Fig. 1. A population of photocarriers with a density modulated at this frequency is generated in the crystal, producing an MPC signal that is amplified and measured by a lock-in amplifier (Stanford Research SR830). The MPC's amplitude I_{ac} and phase shift θ, relative to the phase of the probe beam, are the two main quantities measured in the MPC experiment. An additional photoexcitation by another blue LED, generating a cw light of the same wavelength (the bias beam), is used to create an additional steady-state population of carriers. The modulation amplitude of the probe's intensity is typically not more than 30% of the intensity of the bias beam. The intensity of the bias beam can be varied, so that the additional steady-state photocarrier population and thus the position of the quasi-Fermi level within the band gap are controlled. The changes in the quasi-Fermi level's position are studied in reference to the corresponding changes in MPC spectra of the crystal.

MPC measurements can provide a wealth of information about the interaction of majority carriers with traps and can help in elucidating the relevant transport mechanism and parameters. While varying the modulation frequency ω, one can observe distinct features in the ac photocurrent in the high- and low-frequency domains that can be used to extract the information about the photocarrier transport, including the effect of illumination on the photocarrier mobility, as well as the energetic distribution of trap states within the band gap.

III. RESULTS AND DISCUSSIONS

A. Photoconductivity as a function of incident illumination intensity

The observed dependence of the steady-state photocurrent I_p on the intensity F of incident cw illumination has a form $I_p \sim F^{\alpha}$, with the power exponent $\alpha = 1$ (linear regime) at low illumination intensities, and $\alpha \approx 0.28$ observed at relatively high intensities. See Fig. 2.

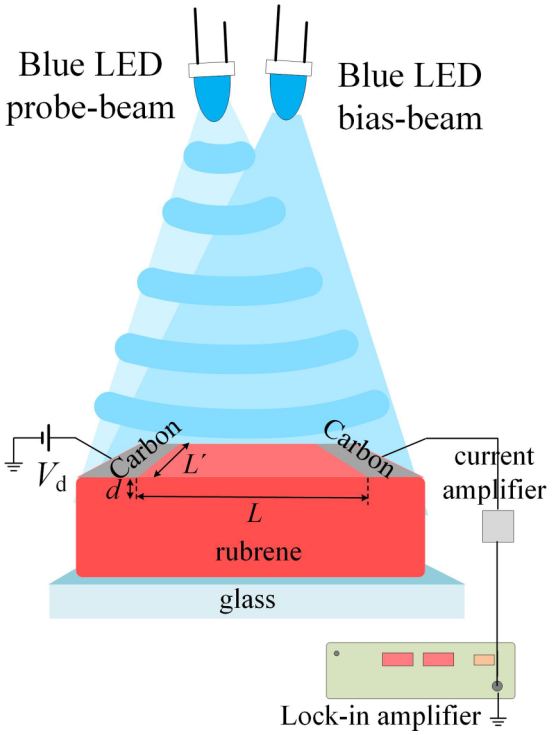

FIG. 1. The modulated-photocurrent (MPC) spectroscopy technique. Two blue LEDs ($\lambda = 460$ nm) are used to photoexcite a rubrene single crystal connected to electric circuitry. The output of the LED on the left is sinusoidally modulated at a frequency ω (the probe beam). The LED on the right provides a steady-state cw photoexcitation (the bias beam). The resultant photoconductivity of rubrene is measured by a lock-in amplifier tuned to the modulation frequency ω of the probe beam. The modulation frequency ω of the probe, as well as the intensity of the bias, can be varied. The effective length, width, and depth (respectively, L, L', and d) of the photoconductive layer contributing to the MPC are indicated (as defined in the text).

When the crystal is briefly exposed to an operating ion gauge in high vacuum (by manually turning the gauge on and off when a sufficiently low pressure is reached), a very rapid decrease of the dark conductivity by a factor of ~ 10 is observed within the first few seconds of the gauge operation. The photoconductivity in the thus prepared "degraded" state of the crystal is also found to be reduced by 1–1.5 orders of magnitude, with the exponent $\alpha = 0.5$ observed in the entire range of studied illumination intensities. The observed power exponents and the gauge effect behavior are in agreement with the previous report by Irkhin *et al.* [14]. We use the gauge effect here to *intentionally* induce surface traps and study the corresponding changes in the crystal's photocarrier transport properties.

B. Spectral response of cw photoconductivity

A spectral response of the photocurrent of a rubrene crystal at a constant excitation intensity of 1 μW is shown in Fig. 3 for pristine, I_p, and degraded, I_p', states of the same crystal. In

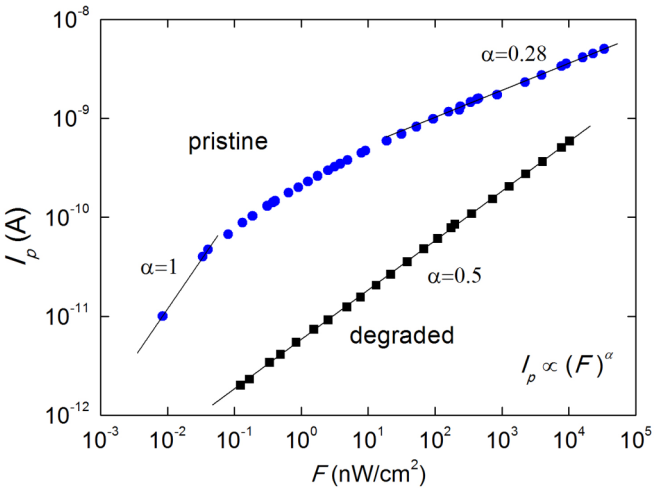

FIG. 2. Photocurrent vs incident light intensity in a rubrene single crystal. Photoexcitation: a blue LED ($\lambda = 460$ nm). A pristine state (blue circles) and a trap-dominated state (black squares) of the same crystal are shown. The trap-dominated ("degraded") state was prepared by exposing the pristine crystal to an operating high-vacuum ion gauge (for 5 s). The photocurrent exhibits a power-law dependence on the incident light intensity, $I_p \sim F^\alpha$, with the power exponent α increasing from $\sim$1 at low intensity to $\sim\frac{1}{4}$ at high intensity for the pristine state of the crystal, and α having a single value of $\frac{1}{2}$ in the trap-dominated state.

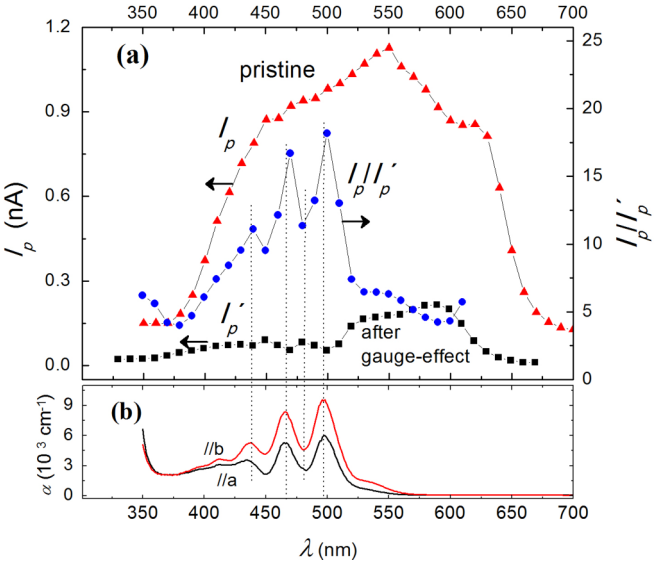

FIG. 3. The photocurrent excitation spectra compared to the absorption spectra of rubrene. (a) Photocurrent excitation spectra of a rubrene crystal in its pristine (red triangles) and trap-dominated (black squares) states. The latter state was prepared by intentionally exposing the crystal to an operating high-vacuum gauge (the "gauge effect"). The ratio of the photocurrents in the pristine and trap-dominated states, I_p/I_p' (blue circles), is also plotted. (b) The experimental absorption coefficient $\alpha(\lambda)$ of rubrene single crystals for light linearly polarized along the crystal's b axis (red) and a axis (black), normally incident on the (a, b) facet of the crystal.

the pristine state, the photocurrent shows two broad maxima around 550 and 620 nm, while other bands corresponding to the vibronic structure of the absorption spectrum of the crystal cannot be discerned. The absence of those other bands in the pristine state can be attributed to a long triplet exciton diffusion length leading to a "smeared" vibronic structure in the photocurrent excitation spectra of rubrene [15]. Moreover, in the pristine state, photogeneration of charge carriers and their transport are believed to occur within a thin photoconductive layer near the surface of the crystals [15].

Following exposure of the crystal to an ion gauge, the photocurrent significantly decreases (Fig. 3) and two small bands with maxima and minima between 450 and 500 nm emerge. The strongest degradation of the photocurrent is observed for wavelengths below 525. It is remarkable that the photoresponse ratio I_p/I_p' (solid blue circles in Fig. 3) reveals sharp maxima occurring at the spectral positions exactly matching the maxima of the absorption spectrum $\alpha(\lambda)$ of rubrene [shown in panel (b)], with the overall spectral shape of this ratio in the region 350–600 nm closely resembling that of $\alpha(\lambda)$. Such behavior is not coincidental: It is an indication that the degradation caused by the gauge is stronger at wavelengths of stronger optical absorption. Namely, the ion gauge leads to a degradation of photoresponse predominately at the optical absorption maxima, where the strong light absorption takes place closer to the surface of the crystal. This observation is reasonable given the fact that exposure to an ion gauge essentially affects the surface of the crystal, thus most strongly affecting the charge transport at or near the surface. The charge carriers generated by strongly absorbed light near the surface undergo recombination within the surface layer, and thus the photocurrent I_p' exhibits a minimum. In contrast, for charge carriers created far from the surface by weakly absorbed light, the recombination probability is lower, and the corresponding photocurrent I_p' exhibits a maximum. These characteristics of the spectrum I_p' of the degraded state demonstrate a bulk character of photoconductivity.

If the photoconductivity of pristine crystals had a conventional (that is, bulk) character, we would expect to see only minor changes in the cw photocurrent shown in Fig. 3, since gauge effect is a short-range phenomenon. The strong degradation of the photocurrent by the gauge effect supports the notion that in pristine crystals, photogeneration of charge carriers and their transport take place in a thin layer at the crystal's surface [14,15]. Following application of the gauge effect, electronic properties of the surface deteriorate, and the surface stops contributing to the net photocurrent. The photocarrier transport is now governed almost entirely by the bulk of the crystal, which is not affected by the gauge effect. This interpretation is further supported by MPC spectroscopy data presented in the following sections.

It is remarkable that a significant photocurrent is generated above 520 nm, where optical absorption abruptly drops. A possible interpretation of this behavior is as follows. In contrast to the region of high optical absorption around 500 nm, where light is absorbed within about 1 μm of the crystal's surface, the low absorption above 520 nm allows for a much deeper light penetration into the bulk, to about 10 μm, and thus leads to a more uniform and diluted density of triplet excitons created via singlet fission. In this case, the average

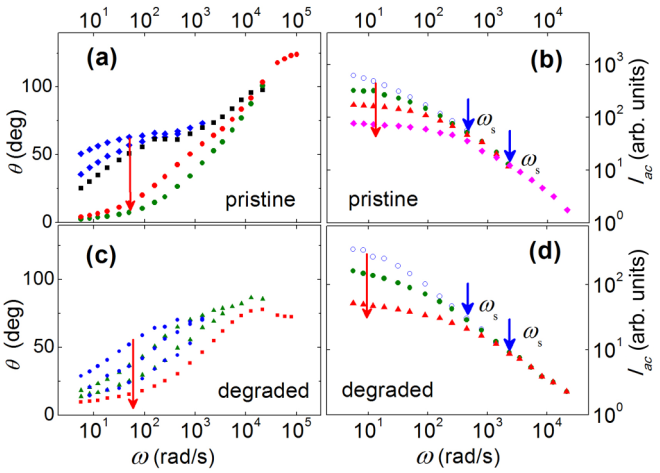

FIG. 4. The MPC spectra of rubrene single crystals. The MPC phase shift θ and amplitude I_{ac} are shown in pristine and trap-dominated (degraded by an ion gauge) states of the same crystal. Panels (a), (b) correspond to the pristine state, while panels (c), (d) correspond to the trap-dominated state of the crystal. The data are plotted as a function of the modulation frequency ω of the probe beam. They are shown for various levels of additional cw bias illumination (corresponding to symbols of different color, with the red arrows pointing in the direction of increasing its intensity). Both the probe and the bias photoexcitations use the same type of blue LED ($\lambda = 460$ nm). There are two regimes evident in these spectra: a low-frequency (LF) regime, in which a nearly zero phase shift and a plateau in the amplitude of MPC are reached, and the high-frequency (HF) regime, where the MPC phase shift is large, and the amplitude is strongly frequency dependent.

separation between triplet excitons becomes greater, leading to a lower probability of triplet-triplet annihilation. Moreover, in the pristine crystal triplet excitons created very deep in the bulk are still able to diffuse to the free surface due to their very long diffusion length in rubrene of several micrometers [15]. Their dissociation at the surface into mobile charge carriers can thus account for the nonzero photocurrent observed in the region of very low absorption above 520 nm.

C. Modulated-photocurrent (MPC) measurements

1. Effect of bias illumination

Figure 4 shows typical MPC phase shift $\theta(\omega)$ and amplitude $I_{ac}(\omega)$ spectra for a rubrene single crystal that initially had a pristine (high-purity) surface [panels (a) and (b)], but was then intentionally degraded by exposure to an operating high-vacuum ion gauge [panels (c) and (d)]. The spectra were collected under photoexcitation with a probe beam ($\lambda = 460$ nm) modulated at a frequency ω, with an additional cw bias photoexcitation of the same wavelength but varied intensity (different levels of bias illumination correspond to symbols of different colors). At high frequencies, the phase θ and amplitude I_{ac} are essentially independent of the bias illumination intensity. At low frequencies, a substantial decrease in both θ and I_{ac} is observed with an increasing intensity of bias illumination (indicated by the red arrows). Although these tendencies in MPC spectra are qualitatively similar to those recently observed in polycrystalline pentacene thin films [11], the results of the data analysis and conclusions drawn here for rubrene are qualitatively and quantitatively different.

Below we first briefly describe the principle of MPC spectral analysis, for which a more detailed theory is given in [10,11], and then analyze the data for rubrene shown in Fig. 4. Considering the general successes and applicability of the *multiple trap and release* (MTR) model of charge transport in organic semiconductors (see, e.g., [16,17]), one can think of the transport of photogenerated carriers as occurring via an ongoing competition between the carrier relaxation from extended (band) states to a distribution of localized in-gap (trap) states and thermal excitation of trapped carriers back into the band. The trap distribution in organic semiconductors usually takes a form of a tail of localized states, extending deep into the gap over considerable energies below the band edge (the so-called *mobility edge*). All energies are usually referred to with respect to this mobility edge. The tail includes both *deep* and *shallow traps* with energies, correspondingly, greater than and smaller than the thermal energy: $E_{deep} \geqslant kT$, and $0 < E_{shallow} \leqslant kT$, where k is the Boltzmann constant, and T is absolute temperature. Considering here for simplicity only *holes* as majority carriers in rubrene and given the high density of states in the highest occupied molecular orbital (HOMO), one can think of charge transport as occurring entirely at a transport energy level matching the HOMO band edge (the mobility edge). It turns out that the contribution of hopping transport in localized tail states can be considered negligible—we will show below that this conclusion is supported by our data. At these conditions, the role of cw bias illumination is to excite carriers across the band gap of rubrene (2.8 eV), thus creating a population of mobile carriers that would quickly relax into the tail of localized states. They will partially fill the tail, starting from deepest levels (deep traps) and up to a certain characteristic energy level E_{tp}, that depends on the density of available photocarriers and trapping cross section. The more photocarriers are generated, the more trap states in the tail are filled, and thus the closer the E_{tp} level gets to the mobility edge. The role of the probe beam, on the other hand, is to selectively probe the contribution of a specific trap level with a characteristic energy E_ω to photoconductivity. Since each trap within the tail is characterized by a certain carrier retention time (or, similarly, the carrier escape rate) that depends on the trap energy, the phase-sensitive detection of ac photoconductivity with a probe beam modulated at a frequency ω predominantly probes the contribution of carriers trapped at and thermally released from the trap of the corresponding energy E_ω. In the MPC measurements, the relative energetic positions of the thus defined energy levels, E_{tp} and E_ω, govern the phase shift and amplitude of MPC spectra.

The rate, e_p, of thermal emission of carriers (holes) from the energy level E_ω at temperature T is

$$e_p(E_\omega) = \frac{2\pi}{\tau_p} = \nu_o \exp\left(-\frac{E_\omega}{kT}\right), \quad (1)$$

where τ_p is the thermal emission time from level E_ω (or, the carrier retention time), and ν_o is the attempt to escape frequency. The rate $e_p(E_\omega)$ can be more generally defined as

$$e_p(E_\omega) = \sqrt{\omega^2 + \omega_t^2}, \quad (2)$$

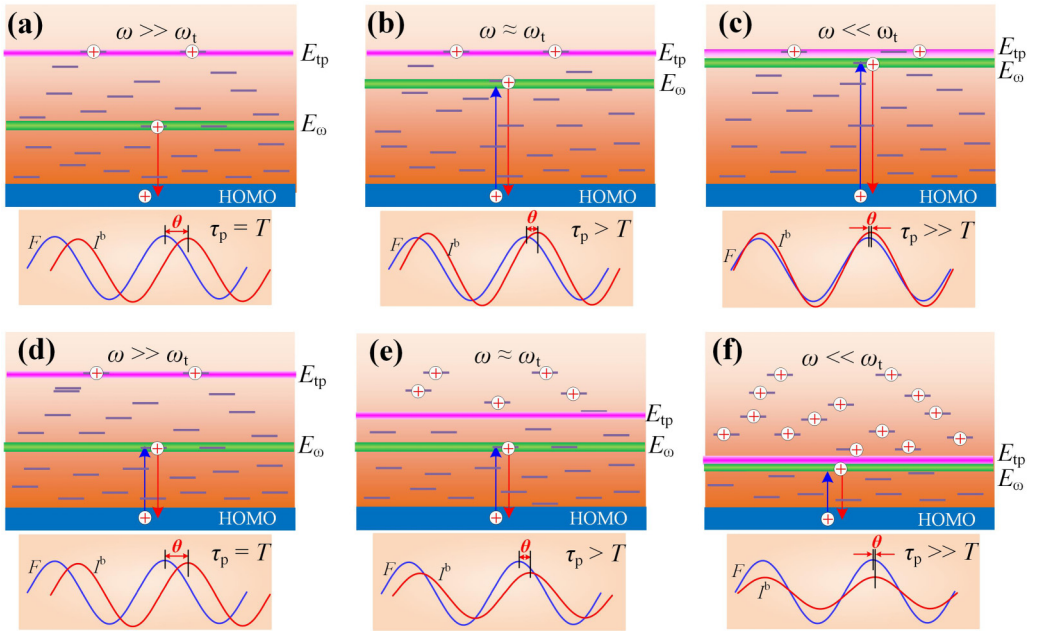

FIG. 5. Illustration of relevant energy levels in MPC spectroscopy. The positions of the probed localized energy level E_ω (the horizontal green line) and the characteristic uppermost filled trap level E_{tp} (the horizontal magenta line) are shown within the band gap of rubrene (orange background) together with other localized (trap) states (short black horizontal lines) and the HOMO edge (the dark blue band). Holes filling the traps up to the E_{tp} level are also shown (white circles with "+" sign). The MPC phase shift θ and amplitude I^b are schematically shown at the bottom of each panel in comparison with the probe beam modulated at a frequency ω. The panels (a)–(c) correspond to a gradual transition from the HF ($\omega \gg \omega_t$) regime in panel (a) to the LF ($\omega \ll \omega_t$) regime in panel (c), occurring with increasing E_ω energy of the probed level (that is, via increasing its depth below the HOMO edge) due to a decreasing frequency of the probe beam ω. In this transition, ω first becomes closer to $\omega_t (\omega \approx \omega_t)$, E_ω shifts closer to E_{tp}, the phase θ decreases, and I^b increases (panel b). At the lowest frequency $\omega \ll \omega_t$, θ becomes negligible, and I^b is high (panel c). Alternatively, the transition from the HF to the LF regime can occur when the intensity of the cw bias illumination increases, as shown in panels (d)–(f). In this case, ω_t becomes closer to ω, E_{tp} level moves closer to E_ω, populating more and more shallow states, and the MPC phase θ and amplitude I^b both decrease (panel e). Eventually, at the highest bias light intensity, the LF regime is reached, when $\omega \ll \omega_t$, E_{tp} matches E_ω, θ is nearly zero, and I^b becomes nearly constant (panel f).

where ω is the modulation frequency of the probe beam, and ω_t is the characteristic trapping frequency given by $\omega_t = pc_p + nc_n$, with p and n representing the steady-state concentrations of mobile holes and electrons (in cm^{-3}) set by the intensity of the cw bias illumination, and c_p and c_n representing the coefficients of carrier capture (in $cm^3\,s^{-1}$) on this specific trap state for holes and electrons, respectively. Recent photo-Hall effect measurements show that photoconductivity of pristine rubrene is fully due to mobile holes, with all the electrons being trapped [18]. Thus, we have

$$\omega_t \cong pc_p, \tag{3}$$

reflecting the fact that ω_t is controlled by the intensity of bias illumination. From Eqs. (1) and (2), the probed energy E_ω is thus given by

$$E_\omega = kT \ln\left(\frac{\nu_o}{\sqrt{\omega^2 + \omega_t^2}}\right), \tag{4}$$

while the quasi-Fermi level corresponding to the upmost filled trap state E_{tp} is

$$E_{tp} = kT \ln\left(\frac{\nu_o}{\omega_t}\right). \tag{5}$$

Therefore, for a given intensity of the bias beam and a given frequency ω of the probe beam, the trap state at E_ω defined by Eq. (4) would provide the maximum contribution to the MPC via a trapping/detrapping processes. At a high probe's modulation frequency ($\omega \gg \omega_t$), ω_t in Eqs. (2) and (4) can be neglected, and the thermal emission rate from the probed state at E_ω becomes equal to the modulation frequency of the probe beam, $e_p(E_\omega) \cong \omega$. Under these conditions, for E_ω and E_{tp} we get

$$E_\omega \cong kT \ln\left(\frac{\nu_o}{\omega}\right), \quad E_{tp} = kT \ln\left(\frac{\nu_o}{\omega_t}\right), \quad \text{and} \quad E_\omega \ll E_{tp}. \tag{6}$$

Expression (6) shows that at $\omega \gg \omega_t$ the probed energy level E_ω corresponds to shallow trap states, located much closer to the band edge than E_{tp}, as schematically illustrated in Figs. 5(a) and 5(d). Correspondingly, all three values—the probed energy level E_ω, the MPC phase shift θ, and amplitude I_{ac}—are nearly independent of ω_t and thus insensitive to the bias beam intensity. This situation corresponds to the high-frequency (HF) regime in the MPC spectra shown in Fig. 4.

When the modulation frequency ω decreases, the MPC spectra exhibit a transition from HF to LF regime, during which the probed energy level E_ω shifts closer to the quasi-Fermi level E_{tp}, as illustrated in Figs. 5(b) and 5(c). Such a transition can be alternatively realized by increasing the intensity of cw bias illumination, thus filling more traps and shifting the E_{tp} level closer to E_ω, as shown in Figs. 5(e)

and 5(f). In this regime, the characteristic frequency ω_t in Eqs. (2) and (4) is no longer negligible, indicating that the trapped holes are thermally emitted from the probed energy level E_ω within a time shorter than the probe beam's modulation period. Thus, holes trapped at E_ω have a comparatively shorter residence time, resulting in a smaller delay of the MPC signal, which accounts for the phase shift θ getting smaller and smaller with decreasing ω [Figs. 4(a) and 4(c)].

Finally, the so-called low-frequency (LF) regime ($\omega \ll \omega_t$) is realized when either a very low probe's modulation frequency ω is used [Fig. 5(c)] or a high bias illumination intensity is applied [Fig. 5(f)]. In this regime, Eqs. (2)–(5) yield $e(E_\omega) \cong \omega_t$, and E_ω and E_{tp} energies become comparable:

$$E_\omega \approx E_{tp} = kT \ln\left(\frac{\nu_o}{\omega_t}\right). \tag{7}$$

Since in this regime the residence time of holes on the probed trap level is negligible compared to the probe beam's modulation period, the delay in MPC signal is negligible, which accounts for the nearly zero phase shift θ at low ω [Figs. 4(a) and 4(b)]. Moreover, in this LF regime, the MPC amplitude I_{ac} becomes almost independent of ω [plateau in Figs. 4(b) and 4(d)], because E_ω is only weakly dependent on ω and barely shifts with varying ω, thus remaining in close proximity to the E_{tp} level, which keeps the I_{ac} signal nearly constant.

2. *Density of free holes, hole mobility, quasi-Fermi energy, and capture coefficient*

The shape of MPC spectra shown in Fig. 4 allows introducing the so-called onset frequency ω_s, defined as the modulation frequency at which a crossover from the HF to the LF regimes starts to occur. This crossover can be seen in $\theta(\omega)$ of pristine rubrene, when the phase starts to decrease with decreasing ω, before it reaches a nearly zero value [Fig. 4(a)].

Alternatively, the crossover can also be identified in $I_{ac}(\omega)$, when the amplitude starts leveling off with decreasing ω, before it reaches a plateau [Fig. 4(b)]. A more accurate method to determine the onset frequency ω_s is presented in Fig. 6 using a typical example of the MPC amplitude $I_{ac}(\omega)$ and $I_{aco}(\omega)$ spectra [Fig. 6(a)] under a cw bias illumination and without it, respectively. It can be seen that the ratio $I_{ac}(\omega)/I_{aco}(\omega)$ in Fig. 6(b), is close to unity (horizontal solid line) at high frequencies, corresponding to the HF regime. At low frequencies, the $I_{ac}(\omega)/I_{aco}(\omega)$ ratio sharply drops following a straight line. The extrapolation of this line intercepts the horizontal solid line at the onset frequency ω_s (indicated by an arrow), defining a crossover from HF to LF regime. The onset of a decrease in $I_{ac}(\omega)/I_{aco}(\omega)$ at ω_s indicates that the characteristic frequency ω_t is a significant fraction of ω_s. Our data suggest that this fraction is roughly

$$\omega_t \approx \frac{\omega_s}{10}. \tag{8}$$

This approximation is supported by the following. The ω_t determined from Eq. (8) can be used to calculate the probe energy level E_ω of the $I_{ac}(\omega)$ spectrum according to Eq. (4), which is plotted in Fig. 6(c) as a function of ω. The

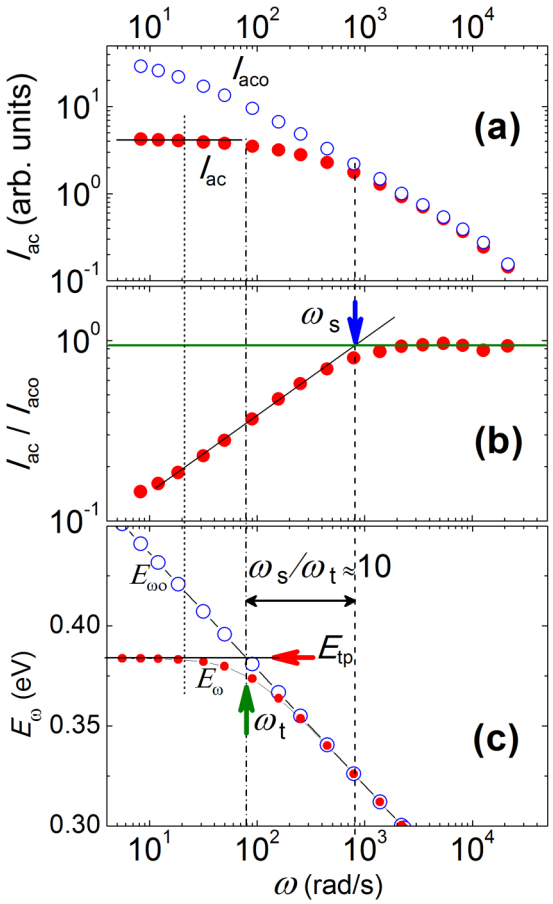

FIG. 6. The method for the determination of the onset frequency ω_s and the characteristic frequency ω_t. (a) Typical MPC amplitude spectra, $I_{ac}(\omega)$ and $I_{aco}(\omega)$, in the pristine state of the crystal under and without cw illumination, respectively. (b) $I_{ac}(\omega)/I_{aoc}(\omega)$ ratio of the spectra in panel (a) used to determine the onset frequency ω_s of the crossover from the HF to the LF regime, which is defined as the intercept of the tilted solid line fitting the $I_{ac}(\omega)/I_{aoc}(\omega)$ data at low ω (transition region) with the horizontal solid line fitting the $I_{ac}(\omega)/I_{aoc}(\omega) \cong 1$ ratio at high ω (HF regime). (c) The probe energy level E_ω of the $I_{ac}(\omega)$ spectrum calculated from Eq. (4) using ω_t estimated from ω_s according to Eq. (8), and the probe energy level $E_{\omega o}$ of the $I_{aco}(\omega)$ spectrum calculated from Eq. (4) assuming negligible ω_{to}.

same plot includes the frequency dependence of the respective probe energy level $E_{\omega o}$ of the $I_{aco}(\omega)$ spectrum without the bias illumination calculated from Eq. (4) considering that the respective ω_{to} is negligible. It can be seen that around ω_s and lower frequencies ($\omega \leqslant \omega_s$) the E_ω level starts to shift more slowly with decreasing ω than the $E_{\omega o}$, accounting for the onset of the drop of the $I_{ac}(\omega)/I_{aco}(\omega)$ ratio and the limit of the onset of HF regime for $\omega \geqslant \omega_s$. In addition, for about $\omega \leqslant \omega_t/4$, the E_ω hardly shifts, indicating that it has essentially reached the respective quasi-Fermi E_{tp} level (horizontal arrow). This is consistent with the fact that in the same spectral region of $\omega \leqslant \omega_t/4$ the $I_{ac}(\omega)$ practically starts to level off [vertical dotted line Fig. 6(a)] showing the characteristic plateau and the onset of the LF regime. In this way, the frequency ω_t defined according to Eq. (8) predicts

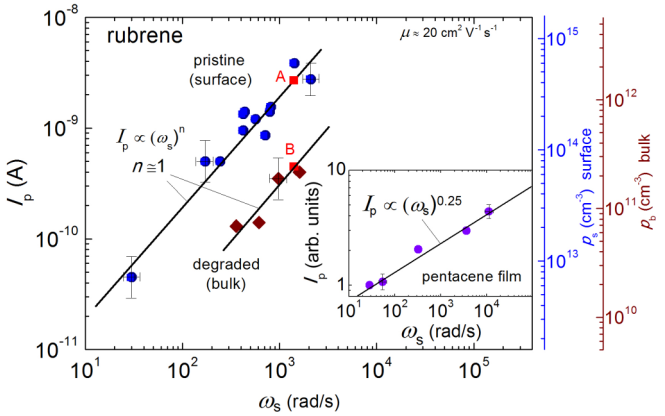

FIG. 7. Dc photocurrent vs MPC onset frequency, $I_p(\omega_s)$, in pristine and degraded rubrene crystals. The solid circles correspond to pristine rubrene single crystal, and the diamonds correspond to the crystal degraded by the gauge effect. The bias illumination intensity ranges between about 0.1 and 10^4 nW/cm^2. It can be seen that an increase of the frequency ω_s by about one order of magnitude roughly corresponds to about one order of magnitude increase of dc photocurrent I_p following the solid line which is the linear fit $I_p \propto (\omega_s)^n$ with $n \approx 1$. The approximate linearity of this relationship suggests that the mobility is carrier-density independent [Eq. (10)]. The inset shows the respective $I_p(\omega_s)$ dependence of pentacene films, which is a sublinear relationship with $I_p \propto (\omega_s)^n$ with $n \approx 0.25$. This is attributed to a decreasing mobility with increasing carrier density due to hole trapping into grain boundaries [11]. The right axis shows indicative values of the free hole densities of the pristine and degraded states calculated from the respective I_p and I_p' according to Eq. (9) for $d_s = 10$ nm and $d_b = 3$ μm.

correctly both the limits of the onset of the HF and LF regimes and so it can be confidently used as a very good approximation of the characteristic frequency ω_t.

Figure 7 presents the dc photocurrent I_p as a function of ω_s obtained by increasing the cw illumination intensity of the pristine (solid circles) and degraded (solid diamonds) states. It is clear from the data in Fig. 7 that the onset frequency significantly shifts to higher frequencies for higher intensities of bias illumination. This occurs due to an increase in the characteristic frequency ω_t, leading to a shift of the quasi-Fermi level E_{tp} to shallower energy levels. Thus, the onset frequency ω_s, which was considered about 10 times higher than ω_t [Eq. (8)], mirrors the movement of the quasi-Fermi level in the gap, which is, in turn, governed by the density of photogenerated carriers. This observation is consistent with the predictions of the MTR model.

It is worth noting that in the hopping transport regime applicable to disordered organic semiconductors, most of the carriers move via *hopping* between localized states. The effect of hopping on MPC spectra was modeled by Longeaud and Tobbeche [19]. It was found that photogenerated excess carriers undergoing hopping transport "condense" in the localized levels around the (dark) Fermi level position. As a consequence, the quasi-Fermi levels are found closer to the position of the dark Fermi level, compared to the case when only MTR is considered, and accordingly the free carrier density decreases. Thus, in a hopping-dominated transport regime, MPC should be almost insensitive to the bias illumination intensity, which would signify the prevalence of hopping transport [19]. This scenario clearly contradicts our experimental observations of the MPC spectral behavior in rubrene single crystals, both in pristine and in trap-dominated states of the crystal, thus ruling out hopping as the dominant transport mechanism. This is a reasonable conclusion, since the present high-quality rubrene crystals demonstrate a remarkable high carrier mobility of up to $\sim$20 cm^2 V^{-1} s^{-1}, which favors a band transport according to the MTR model. For this reason, the present crystals offered an experimental test bed for showing how the modulated-photocurrent measurements can reveal the predominance of a band transport over an incoherent hopping mechanism. This advantage makes MPC spectroscopy powerful in comparison with other experimental techniques, such as a steady-state dark current or steady-state photocurrent measurements that fail to detect the contribution from hopping even in cases when this mechanism is dominant [19].

The onset frequency ω_s is found in Fig. 7 to increase approximately linearly with the concurrently measured dc photocurrent I_p. This is confirmed in the plot of Fig. 7 which contains a large number of data points obtained in pristine rubrene at different levels of bias illumination. From this plot it is evident that an increase of the onset frequency ω_s by about one order of magnitude roughly corresponds to about one order of magnitude increase of the concurrently measured dc photocurrent I_p, indicating that I_p increases approximately linearly with the ω_s as $I_p \propto (\omega_s)^n$, where $n = 1 \pm 0.07$ (solid line). A similar linear dependence of the I_p on ω_s of the respective degraded state is also deduced from Fig. 7 (closed diamonds). The dc photocurrent I_p is proportional to the density-mobility product for mobile holes, $p\mu$:

$$I_p = p\mu eEA, \tag{9}$$

where $E \equiv V/L$ is the applied electric field, determined as the ratio of the applied voltage V to the conduction channel length L. A is the effective cross-section area of the part of the crystal conducting the current, given by $A = L'd$, where L' is the electrode's length and d is the characteristic thickness from the crystal's surface within which the photoconduction takes place (see Fig. 1). When the bias illumination intensity increases, the density of holes p and the characteristic frequency ω_t according to Eq. (3) both increase. This can be monitored as an increasing onset frequency ω_s, because ω_s according to Eq. (8) is considered ten times higher than ω_t. Therefore, the hole density $p = \omega_t/c_p$ should be proportional to ω_s, and the photocurrent I_p should then be proportional to the $\mu\omega_s$ product:

$$I_p \propto \mu\omega_t \propto \mu\omega_s. \tag{10}$$

The linear relationship between I_p and ω_s observed for rubrene (Fig. 7) implies that the hole mobility μ in Eq. (10) remains essentially constant at different intensities of bias illumination. Namely, the mobility appears independent of the carrier p concentration. This contradicts the carrier concentration dependence of the mobility predicted for the hopping transport model in localized states with exponential energy distribution [20], like that of rubrene [21–23] (see also next section). This makes it unlike hopping transport, as was also

concluded from the strong light intensity dependence of the ω_s. Unlike the case of rubrene, similar measurements in polycrystalline pentacene films, which are included in the inset of Fig. 7 for comparison, reveal that an increase of the frequency of ω_s by three orders of magnitude is related to less than one order increase of the concurrently measured I_p. This shows that in pentacene films I_p increases with ω_s sublinearly as $I_p \propto (\omega_s)^n$, where $n \cong 0.25$, which is attributed to a decrease of hole mobility μ with increasing bias illumination intensity. Such behavior in polycrystalline organic films can be explained by hole trapping at grain boundaries that increases the energy barriers for charge transport [11]. It is interesting that carrier trapping at grain boundaries and its effect on the Hall voltage has been recently revealed in Hall effect measurements of high-mobility polycrystalline thin-film organic field effect transistors (OFETS) [24]. Rubrene single crystals are free from grain boundaries, which is consistent with a constant μ observed here in $I_p(\omega_s)$ measurements.

From Fig. 7 the respective plot of I_p vs ω_s (solid diamonds) of the degraded state can be roughly fitted with a similar linear relation $I_p \propto (\omega_s)$ (solid line). This indicates that like the pristine state, the mobility of the degraded state is independent of the bias light intensity. Moreover, the $I_p \propto (\omega_s)$ plot of the degraded state (Fig. 7) is shifted in parallel from the respective plot of the pristine state. Note that this parallel shift could be considered as a vertical downward shift by keeping ω_s constant, due to a possible decrease of the mobility by a factor of 6, if it was considered that a conventional bulk transport phenomenon was also taking place in the pristine state. However, this interpretation is not supported from the recent results of the photo-Hall experiments, which are also based on measurements of the photocurrent using surface electrodes and so measure contributions similar with those of the MPC spectroscopy. The mobility from the photo-Hall was found essentially unchanged showing only a minor increase from the pristine to the degraded state [18]. Therefore the change in the plot of I_p vs ω_s (Fig. 7) by the gauge effect cannot be attributed to a decrease in the mobility. Rather the shift in this plot reflects the induced changes in the probed electronic properties as the effective transport is intentionally switched by turning on the ion gauge from a thin highly photoconductive surface dominating in pristine crystal, to transport in the bulk part of the crystal, dominating the degraded crystal. In this interpretation, in the pristine state the MPC spectroscopy essentially probes the interaction of the charge carriers with the traps in the surface layer. Following the application of the gauge effect the surface layer electronic properties deteriorate due to the creation of traps and a strong decrease of the mobility [18]. Hence the surface layer provides negligible contribution to the photocurrent and the MPC spectroscopy probes the electronic properties of the good quality bulk part of the crystal.

The characteristic thicknesses $d = d_s$ and $d = d_b$, of the effective photoconductive layers of the pristine and degraded states, respectively, are important to calculate the free hole densities and the capture coefficients of the respective probed traps. Specifically, the characteristic thickness d_b is more likely of the order of the absorption length $d = d_b \cong \frac{1}{a} = 3\ \mu$m. For a given photocurrent I_p and the respective turn-on frequency ω_s taken from any given point, for example, point B, of the solid line of Fig. 7 which fits the I_p vs ω_s data of the degraded crystal, the capture coefficient can be determined. Specifically, the free hole density $p_b \approx 1.7 \times 10^{11}$ cm^{-3} is calculated from Eq. (9) considering a mobility $\mu \approx 20\,\text{cm}^2\,\text{V}^{-1}\,\text{s}^{-1}$. Subsequently, from Eqs. (3) and (8) a $c_{pb} \approx 5.7 \times 10^{-10}$ cm^3/s is calculated for the bulk traps. These values, assuming that the effective density of states is $N_v = 10^{21}$ cm^{-3}, give, according to $\nu_o = c_p N_v$, the attempt to escape frequency $\nu_{ob} \approx 5.7 \times 10^{11}$ s^{-1} for the bulk traps.

For the calculation of the respective trapping parameters of the surface layer, the characteristic thickness d_s of the photoconductive surface thin layer is crucial. It is believed that in pristine crystal photogeneration takes place within a thin surface photoconductive layer from the dissociation of triplet excitons which are generated by light absorption deeper in the crystal within the absorption depth ($1/\alpha$). These excitons diffuse up to the surface thin layer where they dissociate by a specific mechanism, which at present is under investigation. Nevertheless, from the recent photo-Hall measurements it is known that under illumination the transport of electrons is completely absent, probably because these are trapped and only the transport of holes is observed [18]. The holes are free to flow from the source to drain, but they are confined within the very thin surface photoconductive layer of characteristic thickness d_s which is expected to be much lower than the light absorption depth. This confinement is because the holes cannot escape toward the bulk part of the crystal, due to the Coulomb attraction from the surface negative charge built up from the trapped electrons following dissociation of excitons [18]. For a given photocurrent I_p of the pristine state taken from the solid line which fits the I_p vs ω_s data of Fig. 7, for example, point A, we have calculated by means of Eq. (9) the free hole density p_s of the surface layer as a function of various possible characteristic thicknesses d_s of the surface layer which is presented in Fig. 8(a). It can be seen that by decreasing the thickness d_s of the surface layers down to 3–10 nm, corresponding to—one to three monolayers, the free hole density p_s increases by several orders of magnitude inversely proportional to the d_s. Based on the so-derived p_s densities, the capture coefficient c_{ps} calculated from Eqs. (3) and (8) and the respective attempt to escape frequency ν_{os} linearly increases with increasing d_s. The relatively much higher density of the p_s for lower d_s requires an analogous, much higher quantum efficiency at the surface layer. As will be shown in the next section, this is supported from the DOS measurements.

3. *Estimating the DOS of localized states from the MPC spectra*

As shown above, the MPC data in the HF regime (Fig. 4) are connected to the density $N(E_\omega)$ of available in-gap states at the probed energy level E_ω given by Eq. (6). The $N(E_\omega)$ density can be obtained as [10]

$$N(E_\omega) = \frac{2}{\pi} \frac{\mu e L' d}{c_p k T} G E \frac{\sin\theta}{I_{ac}}, \tag{11}$$

where $G = (\eta \boldsymbol{\alpha} F)/(h\nu)$ is a photogeneration rate, with F representing the rms of modulated incident illumination intensity (in W cm^{-2}), $\boldsymbol{\alpha}$ is the optical absorption coefficient, $h\nu$ is the photon energy of the probe beam, and η is the quantum efficiency of photocarrier generation. We can estimate an order of

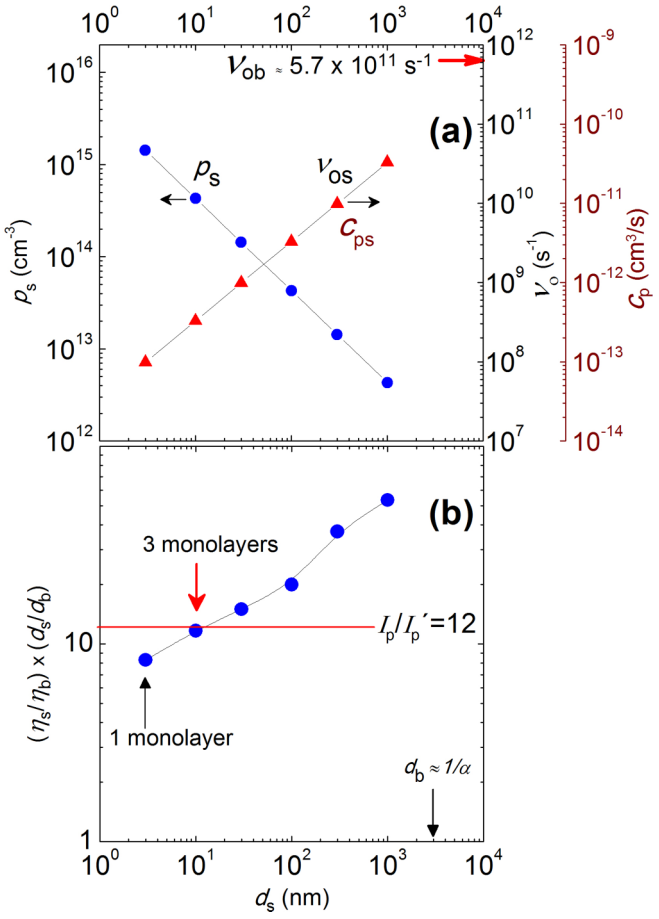

FIG. 8. Dependence on the characteristic thickness d_s of the mobile hole density p_s, attempt to escape frequency ν_{os}, and of the ratio of the quantum efficiency of the surface layer to that of the bulk part of the rubrene crystal. (a) Mobile hole density p_s and attempt to escape frequency ν_{os} for traps in the surface layer. (b) The quantity $(\frac{\eta_s}{\eta_b})(\frac{d_s}{d_b})$ for different characteristic thicknesses d_s of the surface layer.

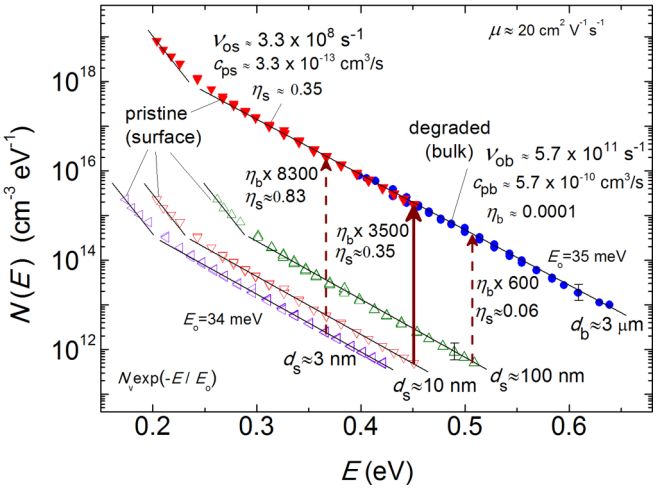

FIG. 9. The density of localized (trap) states, $N(E)$, in pristine and trap-dominated rubrene crystal corresponding to the surface layer with the indicated characteristic thicknesses d_s (closed and open triangles) and the bulk portion (closed circles) of the crystal with characteristic thickness d_b. $N(E)$ is calculated via Eq. (11) using the indicated parameters. The trap-dominated ("degraded") state of the crystal was prepared by briefly exposing the crystal to an operating high-vacuum pressure gauge. Considering higher quantum efficiency by a specific factor shown with the vertical arrows, each DOS of the surface layer with different d_s perfectly matches the DOS of the bulk of the crystal.

magnitude of the DOS of the gap localized states in the crystal assuming a band mobility of $\mu \approx 20\,\mathrm{cm^2\,V^{-1}\,s^{-1}}$, an optical absorption coefficient $\boldsymbol{\alpha} = 3500\,\mathrm{cm^{-1}}$, $d = d_b \cong \frac{1}{a} = 3\ \mu\mathrm{m}$, and the capture coefficient $c_{pb} \approx 5.7 \times 10^{-10}\ \mathrm{cm^3/s}$ derived above for the bulk trap states. The respective $\nu_{ob} \approx 5.7 \times 10^{11}\ \mathrm{s^{-1}}$ derived from the above c_{pb} value is used to calculate the probe energy E_ω level according to Eq. (6). In this way, the only parameter, which is adjusted, is the quantum efficiencyη and so the order of magnitude of the calculated DOS depends upon the choice of η. This parameter should be very low, allowing for the surface layer to demonstrate much higher quantum efficiency and efficient photogeneration of charge carriers essentially within the surface layer of pristine crystal. Indeed, for rubrene crystals very low quantum efficiencies have been reported, $\eta = 0.001$ [15] and 0.0001 [25].

We select the quantum efficiency of $\eta_b = 0.0001$ for the bulk of degraded rubrene crystal. With this value, the magnitude of the DOS of the degraded crystal presented in Fig. 9 (solid circles) is comparable with the respective deep DOS around 0.6 eV obtained earlier in a rubrene field-effect transistor (FET) and space-charge limited current (SCLC) measurements of rubrene crystals [21–23]. A broad, nearly exponential DOS distribution in the form $N_v\exp(-E/E_0)$, with a characteristic slope $E_0 = 35 \pm 1$ meV, is observed at deep energies in the trap-dominated states of the crystal.

Moreover, Blülle [22] reported an exponentially varying deep trap distribution, with almost the same characteristic slope as that in our deep DOS in Fig. 9, indicating that the MPC technique more likely probes the interaction of holes with the trap distribution in the tail of the HOMO band.

Figure 9 also presents the DOS of the pristine state (open symbols) which was calculated from Eq. (11) for various possible characteristic thicknesses d_s of the surface photoconductive layer. For the quantum efficiency η, as a first approximation the same 0.0001 value is assumed as that used for the calculation of the DOS of the bulk part. For the capture coefficient c_{ps} and the attempt to escape frequency ν_{ob}, the values of Fig. 8(a) calculated for the respective d_s values are used. It can be seen from Fig. 9 that the surface layer DOS (open triangles) of the pristine rubrene crystal corresponding to the surface photoconductive layer is unrealistically much lower than the bulk DOS of the degraded crystal (solid blue circles). By decreasing d_s the magnitude of the surface layer DOS remains the same, because the decrease of d_s in Eq. (11) is counteracted by the decrease of c_{ps}, but the DOS shifts in parallel to shallower states due to the decrease of E(ω) from the decrease of ν_{os} in Eq. (6), enhancing the difference from the respective bulk DOS.

It is worth noting that the surface DOS is expected to be at least the same as the bulk DOS or even higher due to possible surface defects. This apparent discrepancy between the surface and bulk DOS indicates that the same low quantum

efficiency 0.0001 value for the whole crystal is not a valid assumption. Assuming for each d_s a properly higher quantum efficiency η_s value than the η_b, the surface layer DOS calculated from Eq. (11) of the pristine state of Fig. 9 (open triangles) can be increased (up arrows) by the factor of η_s/η_b to match the bulk DOS (solid circles). This indicates that the quantum efficiency η_s of the surface layer is much higher than the respective η_b of the bulk part and can account for the relatively higher free hole density p_s than the p_b density.

Specifically, the photocurrents I_p and I'_p of the pristine and degraded states according to Eq. (9) depend on the free hole density, which is proportional to the quantum efficiency η, and on the characteristic effective thickness d of the layer conducting the current ($A = L'd$). Both these parameters η and d are very different in the pristine and degraded states affecting the photocurrent. From the photocurrent excitation spectra of Fig. 3 for the illumination of $\lambda = 460$ nm which is used in the MPC spectroscopy a photocurrent ratio $I_p/I'_p = 12$ is obtained. Since this ratio is obtained for a constant light intensity F and considering that the mobility is not significantly different in the pristine and in the degraded state as deduced from photo-Hall measurements [18], the changes in the η and d from the surface to bulk conducting layers may explain the photocurrent ratio $I_p/I'_p = 12$. This is examined in Fig. 8(b) which presents the product $(\frac{\eta_s}{\eta_b})(\frac{d_s}{d_b})$ for various characteristic thicknesses d_s. This product around $d_s = 10$ nm has decreased very close to the measured ratio of $I_p/I'_p = 12$. This indicates that our data are compatible with a surface thin photoconductive layer with an optimum characteristic thickness of the order of 10 nm, which is about three monolayers. For this d_s, a large ratio $\frac{\eta_s}{\eta_b} = 3.5 \times 10^3$ is deduced from the matching of the surface with the bulk DOS in Fig. 9. However, this ratio is partially counteracted by the respective low ratio $\frac{d_s}{d_b} = 3.3 \times 10^{-2}$, predicting only about 11.7 times decrease in the photocurrent very close to the measured ratio $I_p/I'_p = 12$. Therefore, our data are consistent with the fact that most of the change in the photocurrent induced by the gauge effect is produced from the transfer of the effective transport from a thin photoconductive layer of d_s of the order of 10 nm, to a bulk effective phototransport of $d_b \cong \frac{1}{a} = 3$ μm having more than three orders lower quantum efficiency.

It is worth noting that for the thinner photoconductive layer $d_b \cong 1$ nm (one monolayer), from Fig. 9 it can be seen that the quantum efficiency η_s should be unrealistically high near 83% in order for the surface DOS to match the bulk DOS. Therefore, the surface photoconductive layer probably is not limited to one monolayer, as is the case of the accumulation layer of organic field effect transistors. In addition, if the ten times higher quantum efficiency 0.001 from Ref. [14] was assumed, then ten times higher quantum efficiency η_s values of the surface layer are obtained in order for the surface DOS to agree with the bulk DOS in Fig. 9. In this case, the existence of thin photoconductive layers with $d_s < 100$ nm is questionable, because it requires unrealistically high quantum efficiencies exceeding 100% in order for the surface DOS to match the bulk DOS.

The derived optimum characteristic thickness of $d_s = 10$ nm of the surface layer provides capture coefficient $c_{ps} \approx 3.3 \times 10^{-13}$ cm^3/s and attempt to escape frequency $\nu_{os} \approx 3.3 \times 10^8$ s^{-1}, values that are three orders of magnitude lower than the respective values of the bulk traps derived above. With these values the surface layer DOS of the pristine crystal of Fig. 9 (solid red triangles) calculated with $\eta_s = 0.35$ perfectly overlaps the bulk DOS of the pristine crystal. This indicates very similar exponential DOS distribution for both the surface and the bulk part of the crystal suggesting a surface layer nearly free from extra disorder and traps. In addition, the increase in the steepness of the DOS observed at shallower energies in the pristine state cannot be seen any more in the trap-dominated state, which correlates well with the absence of a sharp upturn in θ at high ω in the degraded crystal [compare panels (a) and (c) of Fig. 4]. This further supports the derived large difference in the magnitudes between the ν_{os} and ν_{ob} since, in this way, according to Eq. (6) the MPC spectroscopy probes different energy regions in the energy gap covering a broad energy region. Specifically, in the pristine state due to the much lower ν_{os}, the MPC spectroscopy probes at higher ω the shallowest $E(\omega)$ levels. These correspond to trap states closer to the band edge where the DOS usually presents a steep upturn, reflecting the commonly observed increase of the DOS near the band edge. At lower ω the MPC spectroscopy probes the onset of the deep exponential distribution. In the degraded state because of the relatively higher ν_{ob} value, the MPC spectroscopy probes the deepest $E(\omega)$ levels of the DOS exponential distribution. In this way, from pristine and degraded states a long exponential DOS distribution is found spanning over five orders of magnitude, from 0.25 eV near the band edge up to 0.65 eV toward the midgap.

IV. CONCLUSIONS

We have studied high-performance organic semiconductors by a modulated-photocurrent spectroscopy technique. This methodology takes advantage of a phase-sensitive detection of photoconductivity induced by a modulated excitation beam, with an additional control by cw background illumination used to tune the mobile carrier density and adjust the position of the quasi-Fermi level within the localized states. In crystalline rubrene, this methodology allowed us to probe the charge transport mechanism, confirming its bandlike nature, and detect changes in the effective transport depth induced by exposure of the crystal to the high-vacuum pressure gauge. The MPC method reveals low but exponential distribution of deep-trap states that becomes steeper at shallower energies. After exposure of the crystals to an operating high-vacuum pressure gauge, a strong decrease in the photocurrent response spectra is observed, which is especially prominent at the wavelengths of the strongest absorption. This behavior indicates that it is the surface layer of the crystal that is predominately affected by the ion gauge via the generation of a substantial additional electronic disorder (traps) at the crystal's surface. Such a disorder drastically limits the surface charge transport, and the main contribution to the photocurrent comes from the bulk of the crystal. In contrast, in the pristine state of the crystal, the main contribution to the photocurrent comes from a thin surface layer. In this interpretation, in pristine rubrene crystals, MPC mainly probes the surface layer, while in the degraded state it probes the

bulk of the crystal. The DOS distribution is found to be the same both for bulk- and for surface-dominated cases, showing that the top surface of the crystal is nearly defect free. The capture coefficient and attempt to escape frequency for hole traps in the bulk are 5.7×10^{-10} s^{-1} and 5.7×10^{11} s^{-1}, respectively. Our data suggest that the characteristic thickness of the photoconductive surface layer of pristine rubrene is of the order of 10 nm (about three monolayers). The surface layer is characterized by more than three orders of magnitude higher photocarrier generation quantum efficiency compared to that in the bulk, which ensures that most photogeneration in pristine crystals essentially takes place at the surface. Moreover, surface traps exhibit a three orders of magnitude lower capture coefficient and attempt to escape frequency, 3.3×10^{-13} cm^3/s and 3.3×10^8 s^{-1}, respectively. This suggests a considerably weaker charge-phonon coupling at the surface of the crystal compared to that in its bulk.

ACKNOWLEDGMENTS

V.P. acknowledges financial support from the National Science Foundation under Grant No. ECCS-1806363. P.K. acknowledges financial support from the Department of Electrical and Computer Engineering, University of Patras.

[1] M. A. Fusella, S. Yang, K. Abbasi, H. H. Choi, Z. Yao, V. Podzorov, A. Avishai, and B. P. Rand, Chem. Mater. **29**, 6666 (2017).
[2] R. A. Nawrocki, N. Matsuhisa, T. Yokota, and T. Someya, Adv. Electron. Mater. **2**, 1500452 (2016).
[3] A. Yamamura, S. Watanabe, M. Uno, M. Mitani, C. Mitsui, J. Tsurumi, N. Isahaya, Y. Kanaoka, T. Okamoto, and J. Takeya, Sci. Adv. **4**, eaao5758 (2018).
[4] M. A. Fusella, A. N. Brigeman, M. Welborn, G. E. Purdum, Y. Yan, R. D. Schaller, Y. L. Lin, Y. L. Loo, T. Van Voorhis, N. C. Giebink, and B. P. Rand, Adv. Energy Mater. **8**, 1701494 (2018).
[5] P. Irkhin, I. Biaggio, T. Zimmerling, M. Döbeli, and B. Batlogg, Appl. Phys. Lett. **108**, 063302 (2016).
[6] L. Basiricò, A. Ciavatti, T. Cramer, P. Cosseddu, A. Bonfiglio, and B. Fraboni, Nat. Commun. **7**, 13063 (2016).
[7] L. Carman, H. P. Martinez, L. Voss, S. Hunter, P. Beck, N. Zaitseva, S. A. Payne, P. Irkhin, H. H. Choi, and V. Podzorov, IEEE Trans. Nucl. Sci. **64**, 781 (2017).
[8] J. Day, S. Subramanian, J. E. Anthony, Z. Lu, R. J. Twieg, and O. Ostroverkhova, J. Appl. Phys. **103**, 123715 (2008).
[9] F. Ortmann, F. Bechstedt, and K. Hannewald, Phys. Status Solidi B **248**, 511 (2011).
[10] M. Pomoni, A. Giannopoulou, and P. Kounavis, Philos. Mag. **90**, 3441 (2010).
[11] N. Vagenas, A. Giannopoulou, and P. Kounavis, J. Appl. Phys. **117**, 033105 (2015).
[12] V. Podzorov, E. Menard, S. Pereversev, B. Yakshinsky, T. Madey, J. A. Rogers, and M. E. Gershenson, Appl. Phys. Lett. **87**, 093505 (2005).
[13] R. W. I. de Boer, M. E. Gershenson, A. F. Morpurgo, and V. Podzorov, Phys. Status Solidi A **201**, 1302 (2004).
[14] P. Irkhin, H. Najafov, and V. Podzorov, Sci. Rep. **5**, 15323 (2015).
[15] H. Najafov, B. Lee, Q. Zhou, L. C. Feldman, and V. Podzorov, Nat. Mater. **9**, 938 (2010).
[16] V. Podzorov, MRS Bull. **38**, 15 (2013).
[17] V. Podzorov, E. Menard, A. Borissov, V. Kiryukhin, J. A. Rogers, and M. E. Gershenson, Phys. Rev. Lett. **93**, 086602 (2004).
[18] V. Bruevich, H. H. Choi, and Vitaly Podzorov, Adv. Funct. Mater. **31**, 2006178 (2021).
[19] C. Longeaud and S. Tobbeche, J. Phys.: Condens. Matter **21**, 045508 (2009).
[20] S. D. Baranovskii, Phys. Status Solidi B **251**, 487 (2014).
[21] B. Blülle, R. Häusermann, and B. Batlogg, Phys. Rev. Appl. **1**, 034006 (2014).
[22] B. Blülle, Doctoral thesis, ETH Zürich, 2016, available at https://doi.org/10.3929/ethz-a-010718150.
[23] J. Dacuña and A. Salleo, Phys. Rev. B **84**, 195209 (2011).
[24] H. H. Choi, A. F. Paterson, M. A. Fusella, J. Panidi, O. Solomeshch, N. Tessler, M. Heeney, K. Cho, T. D. Anthopoulos, B. P. Rand, and V. Podzorov, Adv. Funct. Mater. **30**, 1903617 (2019).
[25] H. Najafov, I. Biaggio, V. Podzorov, M. F. Calhoun, and M. E. Gershenson, Phys. Rev. Lett. **96**, 056604 (2006).